CMS Physics Analysis Summary

Contact: cms-pog-conveners-egamma@cern.ch 2010/03/08

Electromagnetic physics objects commissioning with first LHC data

The CMS Collaboration

Abstract

In this paper we describe the use of the data from the first proton-proton collisions recorded by the CMS detector, at center of mass energy of 900 GeV, to commission the reconstruction of electron and photon physics objects. First comparisons between the data and the simulation of various key ingredients for the reconstruction and identification of electrons and photons are shown. There is good agreement, suggesting a good modeling of the response of the inner tracker and the calorimeters.

1 Introduction

LHC started operation at the end of 2009 and delivered $\sim$ $10\mu b^{-1}$ of integrated luminosity to each of the LHC experiments.

Approximately 200k minimum bias events recorded by the CMS detector [1] at a center of mass energy of 900 GeV were used to commission the reconstruction of the electron and photon physics objects.

All the basic ingredients that contribute to the reconstruction and identification of electromagnetic physics objects were checked: electromagnetic calorimeter (ECAL) and preshower (ES) clusters, the seeding step for electron tracks and the functioning of the dedicated algorithm that is used for electron tracking, the so called 'GSF algorithm', the quality of the reconstructed electron candidates, isolation sums in the tracker, in the ECAL and in the hadron calorimeter (HCAL) as measured around electromagnetic candidates.

It should be noted that, given the low integrated luminosity and the absence of identification requirements, **most of the reconstructed electron and photon objects are due to fakes**, so the comparison is mainly carried out for background. Nevertheless this is still sufficient to assess the general quality and the proper functioning of the algorithms and the modeling of the detector response in the simulation.

2 Datasets and event selection

Minimum bias events are triggered using scintillator planes that are located in front of the Hadron Calorimeter Forward detectors (Beam Scintillator Counters or BSC). The Level 1 trigger requires at least one hit in one of the BSC.

Offline selection is then applied. The requirements are the following:

- the event has to be in time with a valid beam crossing measured by the coincidence of the two beam pickup monitors;
- the BSC beam halo trigger should not be present;
- there should be at least one primary vertex reconstructed with more than four tracks consistent with the beam spot;
- the fraction of *high purity* tracks[2] should be at least 25% for events with at least 10 tracks;
- there should be at least one hit with energy greater than 2 GeV in each of the Forward Hadron calorimeter detectors (HF).

We selected runs where all relevant subdetectors were properly functioning. The selected sample consists of 185330 minimum bias events.

These data are compared to a full MC simulation based on Geant4 [3] of 10M PYTHIA 6.4 [4] minimum bias events. The simulation is carried out using mis-alignments, mis-calibrations and dead channel lists corresponding to the startup conditions of the CMS detector.

3 Clustering studies

3.1 Supercluster reconstruction

Electron and photon showers deposit their energy in several crystals in the ECAL. The presence of material in front of the calorimeter results in bremsstrahlung and photon conversions. Because of the strong magnetic field the energy reaching the calorimeter is spread in ϕ. The energy is therefore clustered at the electromagnetic calorimeter level by building a cluster of clusters (supercluster or SC), which is extended in ϕ, thus minimizing the cluster containment variations due to electromagnetic interactions in the tracker material [5]. The clustering threshold is approximately 1 GeV in transverse energy. ECAL superclusters are used to reconstruct photons and electrons and to drive the selection of tracker seeds for the primary electron tracks in the ECAL seeded electron reconstruction (see section 5).

In this study we concentrate on the raw energy measurement of the superclusters, namely the sum of the energies deposited in the ECAL crystals. In section 3.3 we analyze the response of the preshower detector.

In the data we observe the presence of isolated single crystals that appear to have high energy deposits. Superclusters made of such deposits have substantially different characteristics compared with those arising from standard showers and can be easily identified. In the following such superclusters have been removed using shower shape requirements.

A characteristic of the ECAL is the so called 'Selective Readout' SR. It consists of the full readout of groups of 5x5 crystals corresponding to the trigger towers. When one of the ECAL trigger towers measures a transverse energy larger than 1 (or 2) GeV, all channels in that tower (or in that tower and in the eight towers around it) are read out. In all the rest of the ECAL a zero suppression is applied. During the 2009 data taking, some of the ECAL trigger towers, particularly in the endcaps, were not perfectly timed in and this caused the SR to sometimes not trigger the full read-out even when a region was above threshold. We did not correct the MC to account for this effect and this caused some small discrepancies for variables that are sensitive to very little amount of noise or to negative fluctuations below the pedestal.

3.2 Supercluster data-MC comparisons

In this subsection we present data-MC comparison for the kinematic and shower shape variables of the SCs.

SCs are selected with the following requirements:

- the SC η must satisfy $|\eta| < 1.4442$ and $1.566 < |\eta| < 2.5$, avoiding the transition region between barrel and endcaps.
- the raw SC E_t must be greater than 2 GeV.

In total 3226 SCs satisfy these requirements in the data. Of these, 2120 are reconstructed in the barrel while 1106 in the endcap. In the following plots the Monte Carlo is normalized to the total number of SCs observed in the data, in case of barrel/endcaps plots two different normalizations have been used.

Figure 1 shows the distributions for data and Monte Carlo of the number of superclusters per event and of the supercluster raw E_t. Figure 2 shows the distributions for data and Monte Carlo as a function of the pseudorapidity of the SC. Figures 3 and 4 show two shower shape variables: the ratio between the maximum crystal energy and the total energy of the 5x5 crystal array centered around the maximum energy crystal and the ratio between the sum of the crystals

in the two neighboring 1x5 eta strips, labeled as 2x5, containing the shower and the same 5x5 crystal array sum. This ratio may be larger than one due to fluctuation of the electronic noise to the lower side of the pedestal for crystals in regions that are fully read out.

Figure 5 shows the distribution of R9: the ratio of the energy contained in the 3x3 region around the seed crystal and the total supercluster energy. R9 is used to discriminate between converted and unconverted photons [5]. R9 is sometimes larger than one for the reason given above. Figure 6 shows the distribution of H over E: the ratio of the energy in the HCAL behind the SC and the energy of the SC itself. For HCAL, only towers with energy greater than 0.7 and 0.8 GeV are considered in the sum respectively for barrel and endcaps.

All shape variables in the endcaps show some discrepancy between data and MC for values larger than one, due to the SR issues described in subsection 3.1. Apart from this, good agreement is observed for all the variables considered.

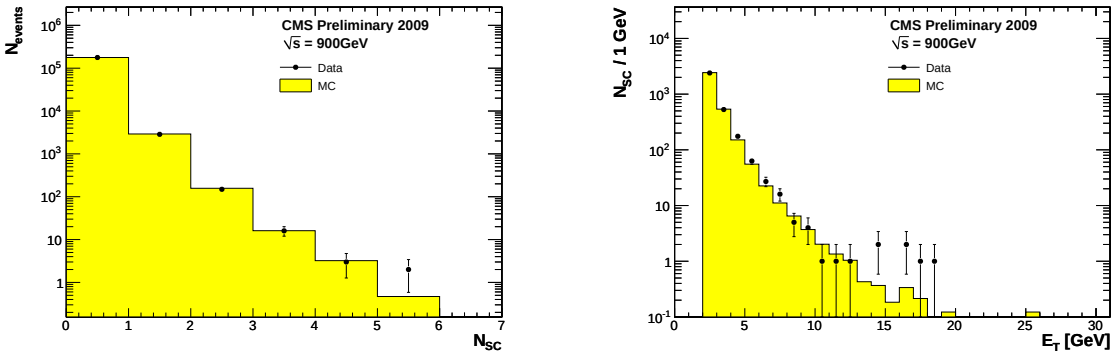

Figure 1: Number of selected superclusters per event (left) and raw Supercluster transverse energy distribution (right). The black points correspond to data and the histogram to simulated minimum bias events.

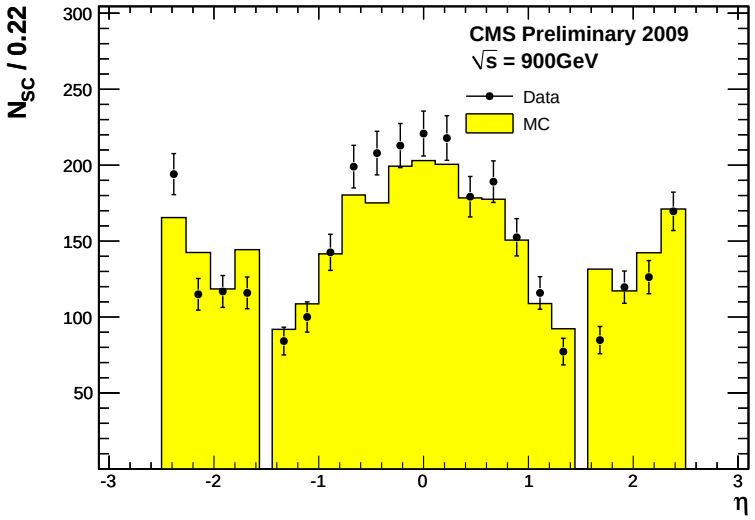

Figure 2: Pseudorapidity distribution of the superclusters. The black points correspond to data and the histogram to simulated minimum bias events.

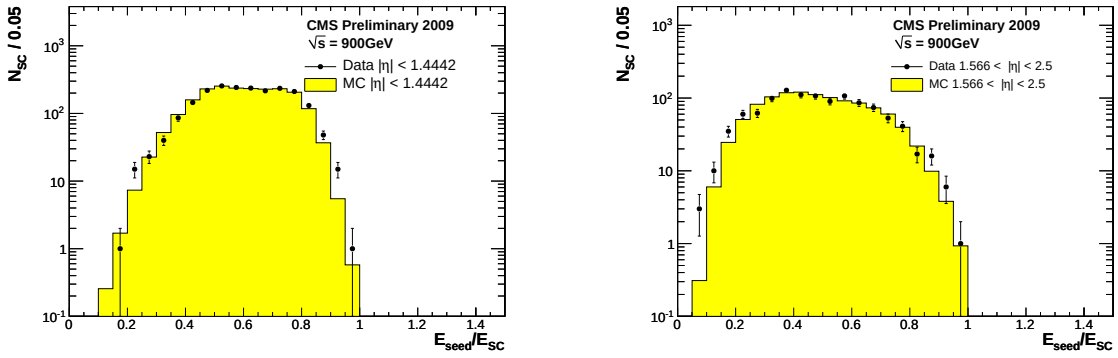

Figure 3: Ratio between the most energetic crystal energy and total supercluster energy for the barrel (left) and endcaps (right) SCs. The black points correspond to data and the histogram to simulated minimum bias events.

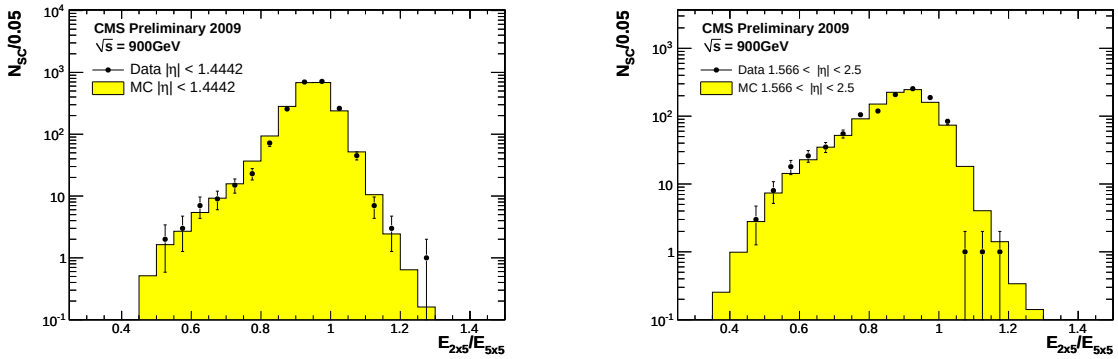

Figure 4: Ratio between the energy contained in the 2x5 crystal eta-strip and the energy in the 5x5 crystal array for the barrel (left) and endcaps (right) SCs. The black points correspond to data and the histogram to simulated minimum bias events.

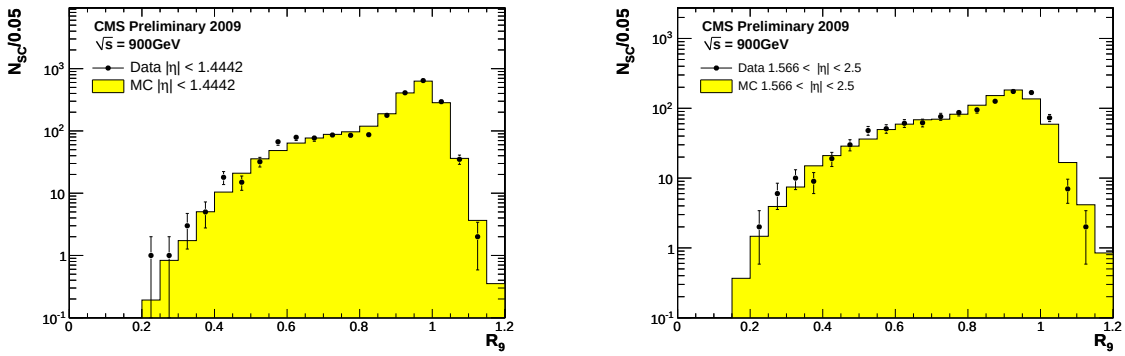

Figure 5: R9: ratio between the energy contained in the 3x3 region around the seed crystal and the total supercluster energy for the barrel (left) and endcaps (right) SCs. The black points correspond to data and the histogram to simulated minimum bias events.

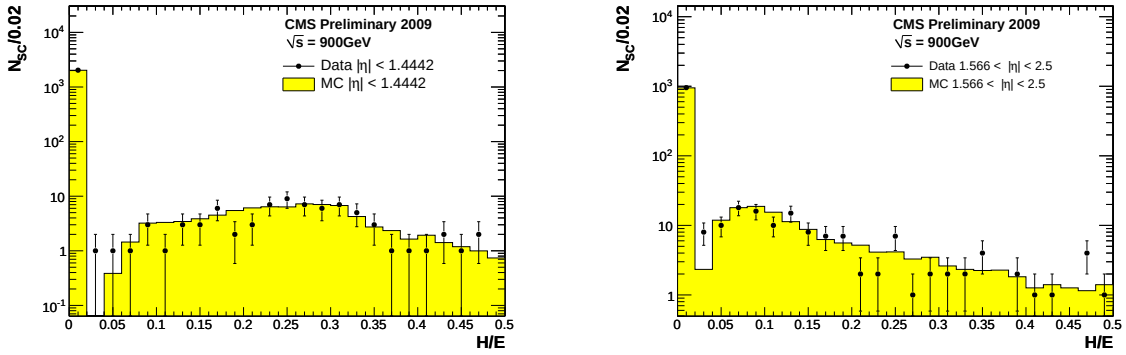

Figure 6: H over E distribution for SCs in the barrel (left) and endcaps (right). The black points correspond to data and the histogram to simulated minimum bias events.

3.3 Preshower data-MC comparisons

The preshower detector (ES) is located in front of the ECAL endcaps and covers the $1.65 < |\eta| < 2.6$ region. Figures 7 and 8 show the energy ratio of the 2^{nd} to the 1^{st} ES plane and the energy of preshower clusters in the two planes expressed in MIPs. The preshower clusters are associated to ECAL superclusters with raw transverse energy larger than 2 GeV and $|\eta| < 2.5$. We also checked that the individual distributions observed in the two endcap halves are consistent with each other.

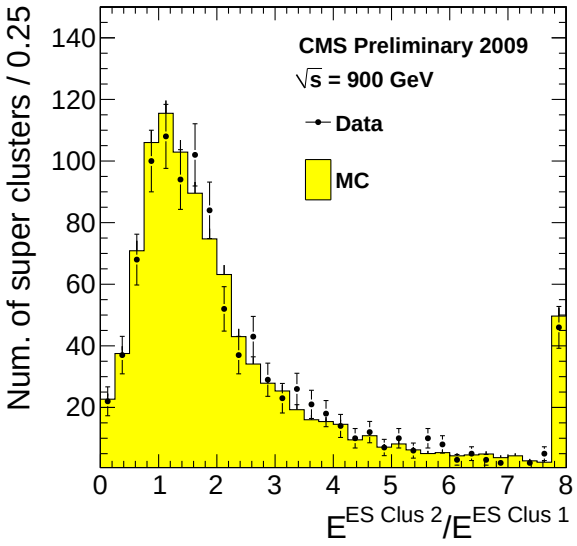

Figure 7: The ratio of the energy deposit associated with a supercluster on the second ES plane to the first one for supercluster raw transverse energy larger than 2 GeV. Overflows are added to the last bin.

4 Gsf tracking studies

The standard CMS track reconstruction is based on the Kalman Filter (KF) and relies on Gaussian probability density functions. This is not the optimal reconstruction algorithm for electron tracks, whose expected energy loss has a long non Gaussian tail due to radiative interactions

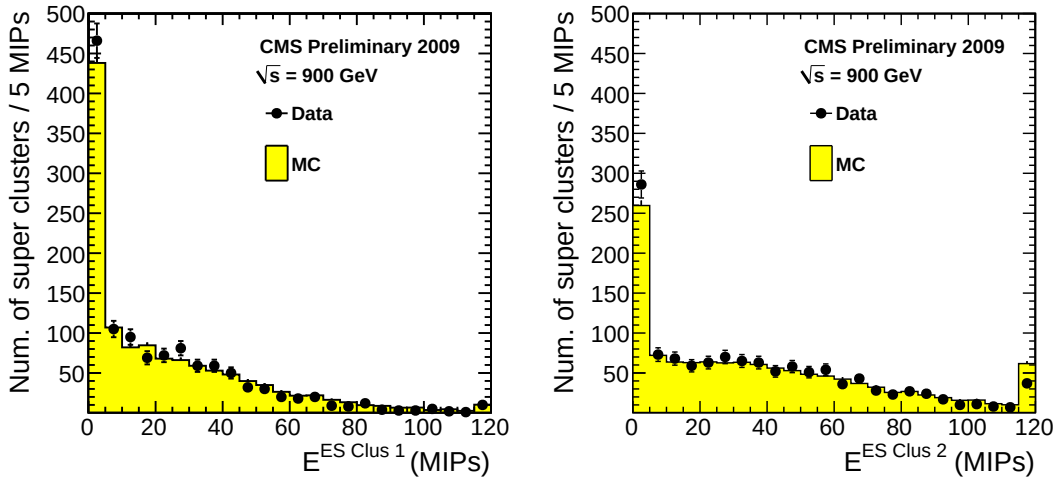

Figure 8: Energy deposited in each of the two ES planes for supercluster raw transverse energy larger than 2 GeV. Overflows are added to the last bin.

of electrons in the tracker material. A Gaussian-sum filter (GSF) algorithm for electron track reconstruction in the CMS tracker has been developed and implemented [6]. The GSF tracking algorithm, being able to follow the change of curvature of the electron track, allows to obtain an unbiased estimate of the track momentum at both track ends. This procedure also allows for a tracker measurement of the fraction of energy lost by bremsstrahlung, defined as $f_{brem} = (p_{in} - p_{out})/p_{in}$ [7]. This variable plays an important role in the electron reconstruction and identification and it is useful to verify the effectiveness of this variable, comparing its distribution with the simulation. In particular it gives the ability to spot eventual problems in the behavior of the GSF algorithm or in the parametrization used to model the amount of material in the tracker. In the following all GSF quantities are determined by their mode.

The number of reconstructed GSF tracks using the electron seeding is rather small so, to increase the statistics, GSF tracks were reconstructed for all the available tracking seeds.

Tracks are then required to satisfy the following criteria:

- the tracks should have at least 7 hits.
- GSF tracks are required to be matched to *high purity* KF tracks that are reconstructed using the first two iterations of the track reconstruction (i.e. seeded by pixel triplet and pair seeds) [2] and have a p_t larger than 1.5 GeV/c. The matching has been done by requiring that the two tracks have at least 50% of shared hits (fraction computed on the shortest track).

A total number of 99261 tracks are selected in the data of which 65642 with $|\eta| < 1.479$, pointing to the ECAL barrel. In all following plots the Monte Carlo is normalized to the total number of selected tracks in data for each pseudorapidity range independently and underflows and overflows are added to the first and last bin respectively.

Fig. 9 shows the f_{brem} distribution of the GSF tracks in data and Monte Carlo in three η ranges corresponding to different parts of the tracker. As expected, since most of the tracks are fake electrons (i.e. pions), the distribution is peaked at $f_{brem} = 0$ with tails on both sides mainly due to fluctuations in the p_{in} and p_{out} measurement.

Fig. 10 shows the ratio of the inner momentum of the GSF tracks to the KF momentum in data

and Monte Carlo in the same η intervals. We can see from the figures that the agreement is very good for $|\eta| < 2$ while for larger pseudorapidities we observe some shift in the data towards higher f_{brem} values compared to MC expectations.

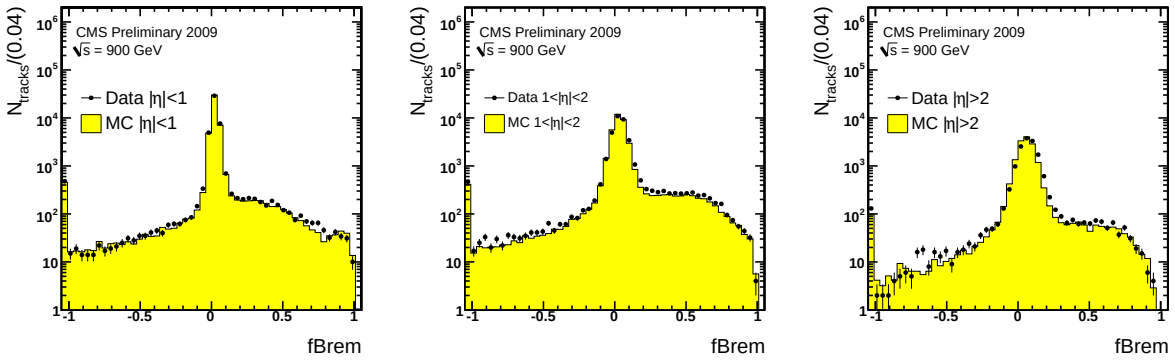

Figure 9: f_{brem} for *high purity* GSF Tracks in data (dots) and MC (solid histogram). The three plots correspond to different pseudorapidity ranges. In each plot the MC is normalized to the total number of selected tracks in data and underflows and overflows are added to the first and last bin respectively.

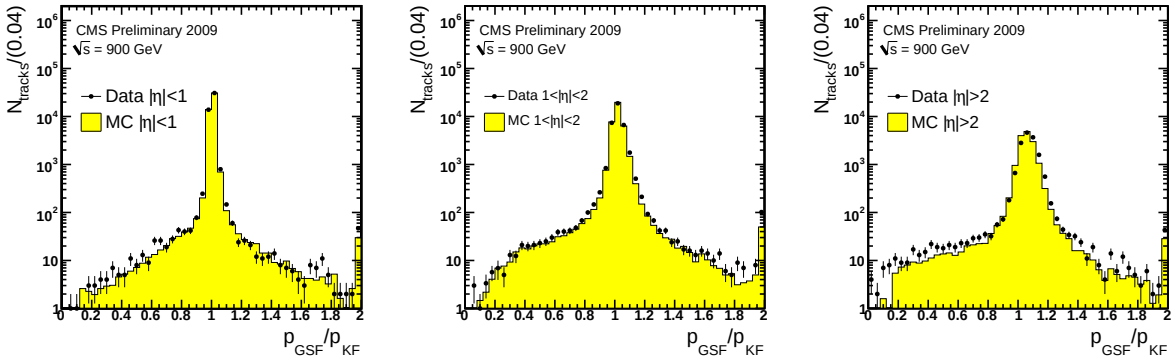

Figure 10: Ratio between the GSF track p_{in} momentum and the momentum of the associated KF track. Data are represented as dots, MC as a solid histogram. The three plots correspond to different pseudorapidity ranges. In each plot the MC is normalized to the total number of selected tracks in data and underflows and overflows are added to the first and last bin respectively.

5 Electron studies

Electrons are reconstructed using two complementary algorithms at tracking seeding stage: 'ECAL driven' [7] and 'tracker driven'. The 'ECAL driven' algorithm is seeded by ECAL SCs of $E_t > 4$ GeV and is optimised for isolated electrons in the p_T range relevant for Z or W decays and down to $p_T \simeq 5\ GeV/c$, and is complemented by the 'tracker driven' seeding more suitable for low p_T electrons as well as performing better for electrons inside jets.

In the collected minimum bias sample, only very low p_T electron candidates are expected. The sample of electron candidates is predicted to be dominated by charged hadrons or electrons coming from photon conversions. In the simulation, a total of 33.9% of the reconstructed can-

didates are found to be matched to a generator level electron (4.6%) or photon (29.3%) in a cone of $\Delta R = 0.15$.

As a first step, results on the ECAL seeding are presented. They are obtained by performing a special reconstruction where the cuts applied in the matching between ECAL clusters and tracker seeds are relaxed. The windows for matching with the pixel hits are increased by approximately a factor 10 to study the tails of distributions.

Figure 11 shows the distributions of the differences between the expected position and the hit position in the second pixel (strip) layer for the electron candidates. Distributions are shown for both $r - z$ and ϕ coordinates and separately for barrel pixel layers and for forward layers (pixels and strips). The Monte Carlo distributions are normalized to the total number of electron candidates in the data. The Monte Carlo expectation for electron candidates matched to a generated electron or γ is also shown. The distributions from the data and the Monte Carlo are found to be in good agreement.

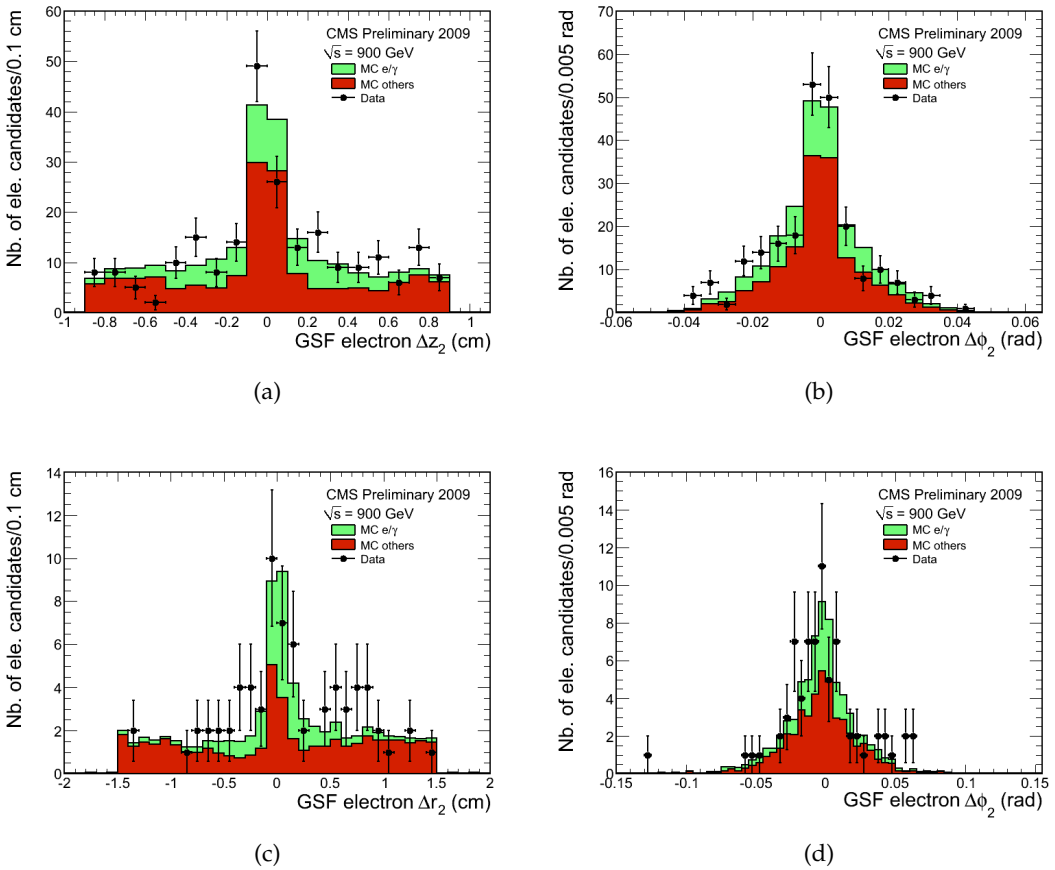

Figure 11: Differences Δz_2 (or Δr_2) and $\Delta\phi_2$ between measured and predicted hit position on the second layer for the ECAL driven seeding with the relaxed matching windows: (a) pixel barrel, z coordinate (b) pixel barrel, ϕ coordinate (c) pixel and strip forward, r coordinate (d) pixel and strip forward, ϕ coordinate. The Monte Carlo distribution is normalized to the total number of electron candidates in the data. The Monte Carlo expectation for electron candidates matched to a generated electron or γ is also shown (filled green histogram).

The standard selection of electron candidates at reconstruction level consists of cuts at seeding level and of a preselection. This selection differs between ECAL seeded and tracker seeded

reconstructed electrons. The 'ECAL driven' seeding algorithm uses cuts on the supercluster corrected transverse energy (4 GeV) and on the ratio H over E of the hadronic energy behind the supercluster over the supercluster energy. For candidates found by the 'ECAL driven' seeding algorithm, the selection performed at the seeding level is complemented by a preselection based on the matching between the GSF track and the supercluster in η and ϕ. For candidates found only by the 'tracker driven' seeding algorithms, the preselection is based on a multivariate analysis as described in [8].

Table 1 presents the number of electron candidates found in the data in the ECAL barrel and in the ECAL endcaps. The number of candidates found by the ECAL driven and found by the tracker driven algorithms are also indicated.

	EB+EE	EB	EE
Nb. electron candidates	351	210	141
ECAL driven	60	43	17
Tracker driven	317	186	131
Nb. electron candidates, $E_T > 4\ GeV$	74	47	27
ECAL driven, $E_T > 4\ GeV$	60	43	17
Tracker driven, $E_T > 4\ GeV$	40	23	17

Table 1: Number of electron candidates in the data and in the ECAL barrel (EB) or ECAL endcaps (EE). Numbers are also given separately for the electron candidates found by the ECAL driven and by the tracker driven algorithms, for all E_T and for $E_T > 4\ GeV$.

In all the following plots the Monte Carlo datasets are normalized to the number of electron candidates measured in the data.

At low p_T most of the candidates are reconstructed from the tracker driven algorithm as shown in Figure 12. The relative fraction of electron candidates found by the 'ECAL' or the tracker driven seeding algorithm is well reproduced by the simulation even at such low energies.

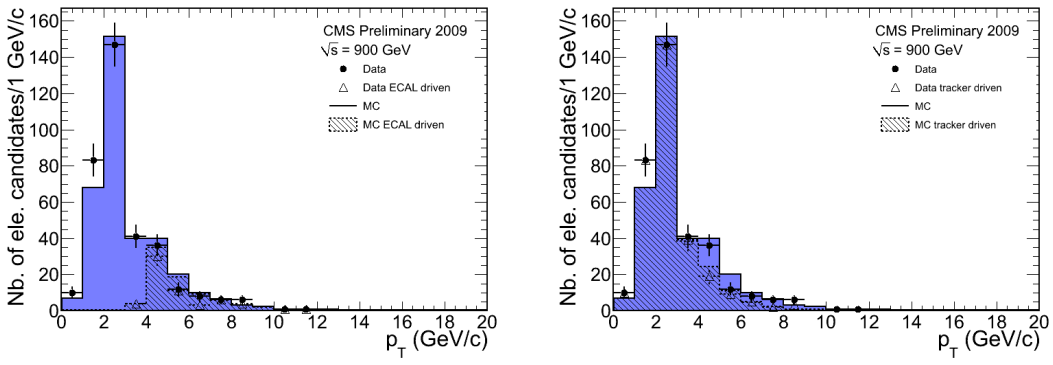

(a) (b)

Figure 12: Distribution of the electron candidates transverse momentum in the data (dots) compared to the Monte Carlo (filled blue histogram). The Monte Carlo distribution is normalized to the total number of electron candidates in the data. The contributions of electron candidates found by the ECAL driven algorithm (a) and of those found by the 'tracker driven' algorithm (b) is shown with triangles for the data and hatched histogram for the MC.

Figures 13 and 14 show the kinematic distributions of the electron candidates p_T and η respectively. Figures 15, 16 and 17 show the distributions of E/p and of the position matching $\Delta\eta_{in}$ and $\Delta\phi_{in}$ between the GSF track and the SC. The track position is obtained by extrapolating from the innermost track state toward the energy weighted position of the SC. The double peak structure in $\Delta\phi_{in}$ is expected and is due to the helix extrapolation performed inside the ECAL which leads to a bias at very low p_T whose sign depends on the electron charge. At higher p_T the effect is negligible and no bias is expected.

Figure 18 shows the distribution of the bremsstrahlung fraction f_{brem} of the electron candidates.

Figure 19 shows the distribution of the distance of closest approach of the reconstructed electron track to the beam spot position in the transverse plane. In all figures, the Monte Carlo contribution of electron candidates matched to a generated electron or γ is also shown. A general good agreement is observed for all the considered variables.

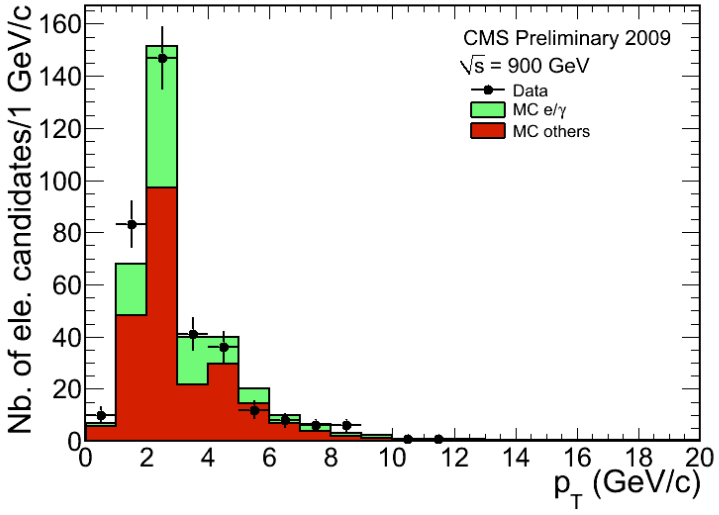

Figure 13: Electron candidate transverse momentum in the data (dots) compared to the Monte Carlo (filled histogram). The Monte Carlo is normalized to the total number of electron candidates in the data. The Monte Carlo expectation for electron candidates matched to a generated electron or γ is also shown (filled green histogram).

6 Isolation studies

Isolation variables for superclusters and reconstructed electrons were compared between data and simulation. We have considered the following isolation variables:

- *Track isolation*: the sum of the transverse momenta of Kalman Filter tracks that are reconstructed in a hollow cone around the reconstructed object. The dimensions of the cone are $0.04 < \Delta R < 0.3$. Only tracks with transverse momentum greater than 0.7 GeV are considered in the sum.
- *ECAL isolation*: the sum of the transverse energy reconstructed in individual channels of the ECAL in a cone around the reconstructed object with outer cone sizes $\Delta R = 0.3$ or $\Delta R = 0.4$ and inner cone radius corresponding to the size of 3 ECAL crystals ($\Delta R \sim 0.05$ in barrel region). The transverse energy in channels that are

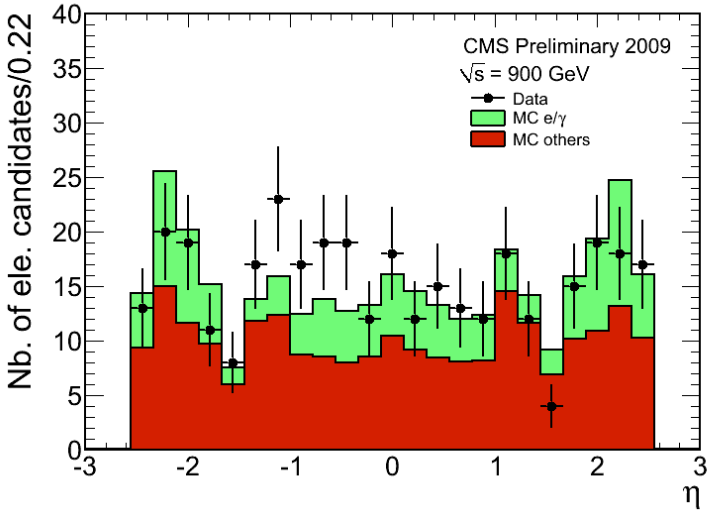

Figure 14: Electron candidates pseudorapidity in the data (dots) compared to the Monte Carlo (filled histogram). The Monte Carlo is normalized to the total number of electron candidates in the data. The Monte Carlo expectation for electron candidates matched to a generated electron or γ is also shown (filled green histogram).

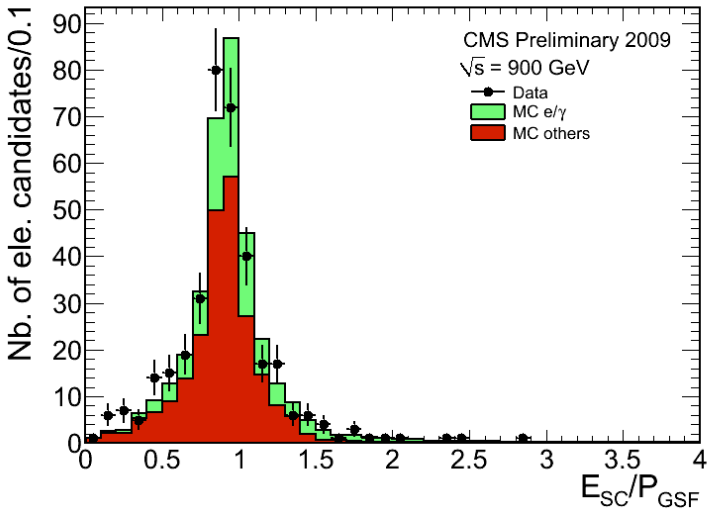

Figure 15: Ratio E/p between the supercluster energy and the GSF track momentum in the data (dots) compared to the Monte Carlo (filled histogram). The Monte Carlo is normalized to the total number of electron candidates in the data. The Monte Carlo expectation for electron candidates matched to a generated electron or γ is also shown (filled green histogram).

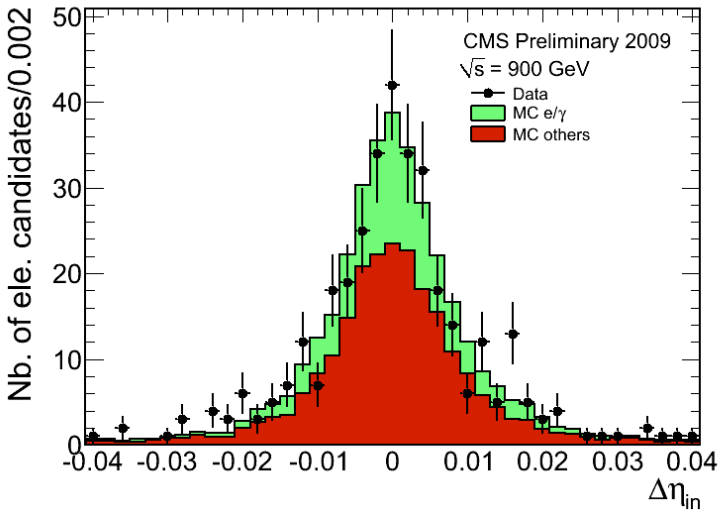

Figure 16: Difference $\Delta\eta_{in}$ between the supercluster position and the track extrapolation from the innermost measurement in the data (dots) compared to the Monte Carlo (filled histogram). The Monte Carlo is normalized to the total number of electron candidates in the data. The Monte Carlo expectation for electron candidates matched to a generated electron or γ is also shown (filled green histogram).

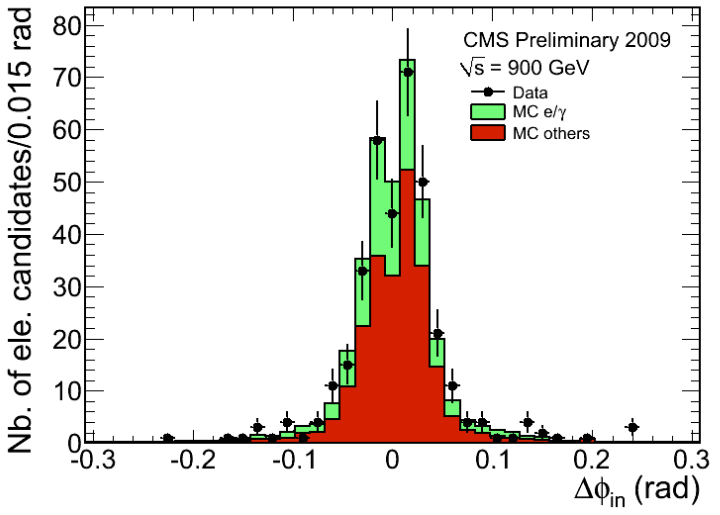

Figure 17: Difference $\Delta\phi_{in}$ between the supercluster position and the track extrapolation from the innermost measurement in the data (dots) compared to the Monte Carlo (filled histogram). The Monte Carlo is normalized to the total number of electron candidates in the data. The Monte Carlo expectation for electron candidates matched to a generated electron or γ is also shown (filled green histogram).

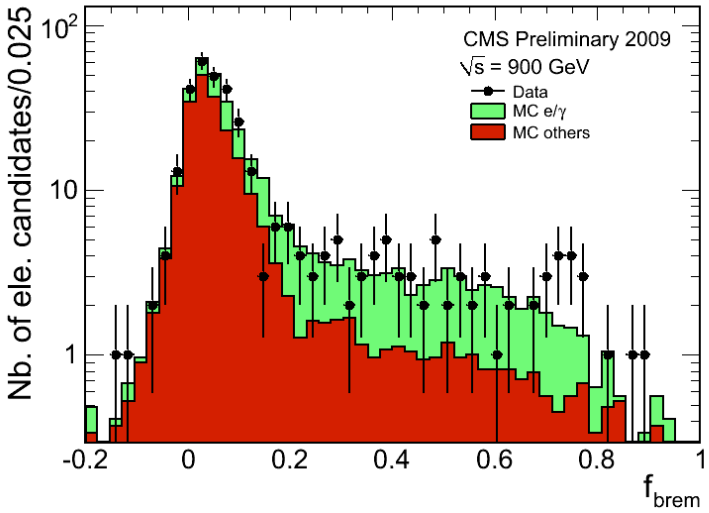

Figure 18: Relative difference $f_{brem} = (p_{in} - p_{out})/p_{in}$ between the track momentum estimate at the innermost and at the outermost position in the data (dots) compared to the Monte Carlo (filled histogram). The Monte Carlo is normalized to the total number of electron candidates in the data. The Monte Carlo expectation for electron candidates matched to a generated electron or γ is also shown (filled green histogram).

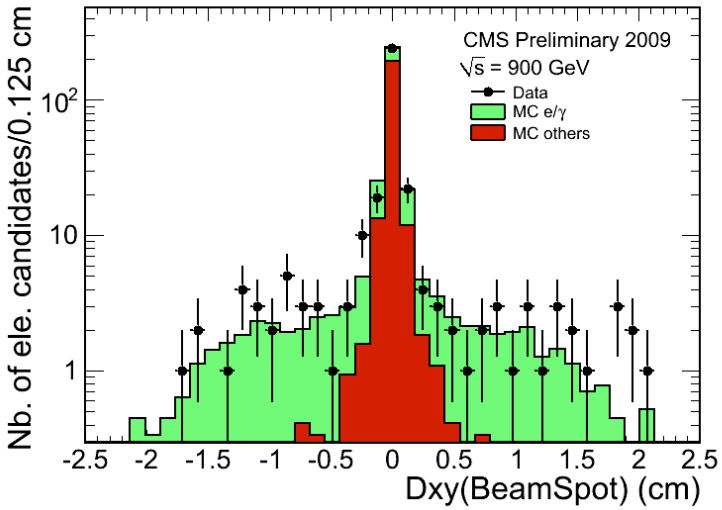

Figure 19: Distance of closest approach to the beam spot in the transverse plane in the data (dots) compared to the Monte Carlo (filled histogram). The Monte Carlo is normalized to the total number of electron candidates in the data. The Monte Carlo expectation for electron candidates matched to a generated electron or γ is also shown (filled green histogram).

found in a strip along ϕ centered at the ECAL position of the reconstructed object with an η-width of 3 crystals are also not considered in the sum. Only those reconstructed hits with the absolute value of the energy greater than 0.08 GeV in the ECAL barrel (EB) and with the absolute value of the transverse energy of 0.1 GeV in the ECAL endcaps (EE) are considered. The cut on the absolute value of the energy is aimed at averaging out the effect of noise and it may give rise to negative values of the ECAL isolation variable. A filtering is applied too, aimed at removing single channels, similar to what has been described in section 3.

- *HCAL isolation*: the sum of the transverse energy of HCAL towers in the region behind the ECAL cluster of the reconstructed object. The sum is performed in a cone with dimensions $0.15 < \Delta R < 0.3$ or 0.4. The energy is summed of towers which have an energy greater than 0.7 GeV in the barrel and 0.8 GeV in the endcap.

6.1 Supercluster isolation

In all plots the Monte Carlo sample is normalized to the number of superclusters in data, in case of barrel/endcaps plots two different normalizations have been used.

Superclusters were selected with the same requirements described in section 3.

Fig. 20 shows the track isolation, Fig. 21 shows the ECAL isolation and Fig. 22 shows HCAL isolation computed for the selected superclusters.

All isolation variables present a good agreement between data and Monte Carlo.

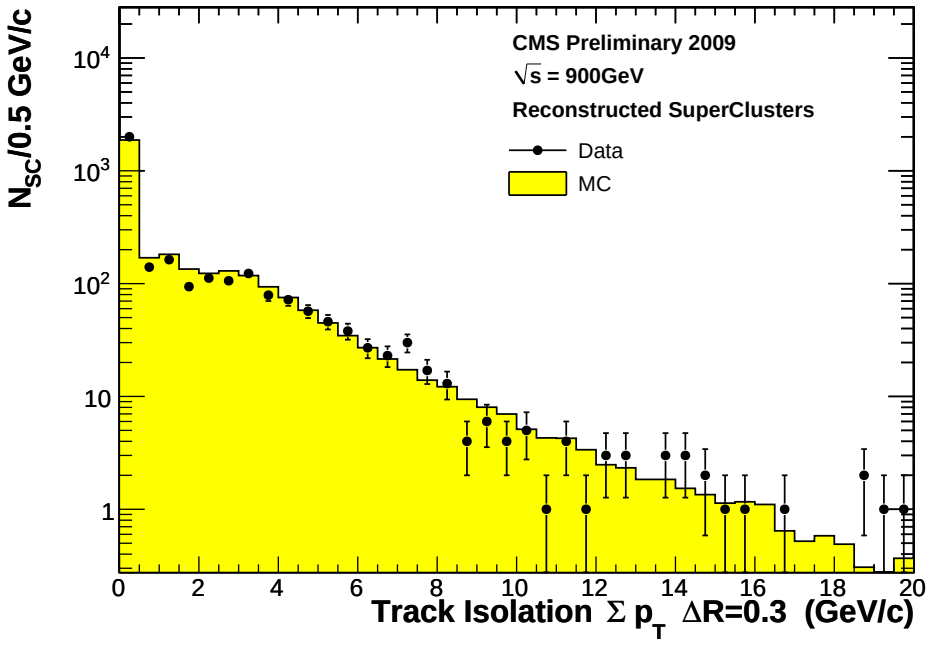

Figure 20: Track isolation distribution for superclusters. The black points correspond to data and the histogram to simulated minimum bias events.

6.2 Electron isolation

In all plots the Monte Carlo sample is normalized to the number of reconstructed electron candidates in data, in case of barrel/endcaps plots two different normalizations have been

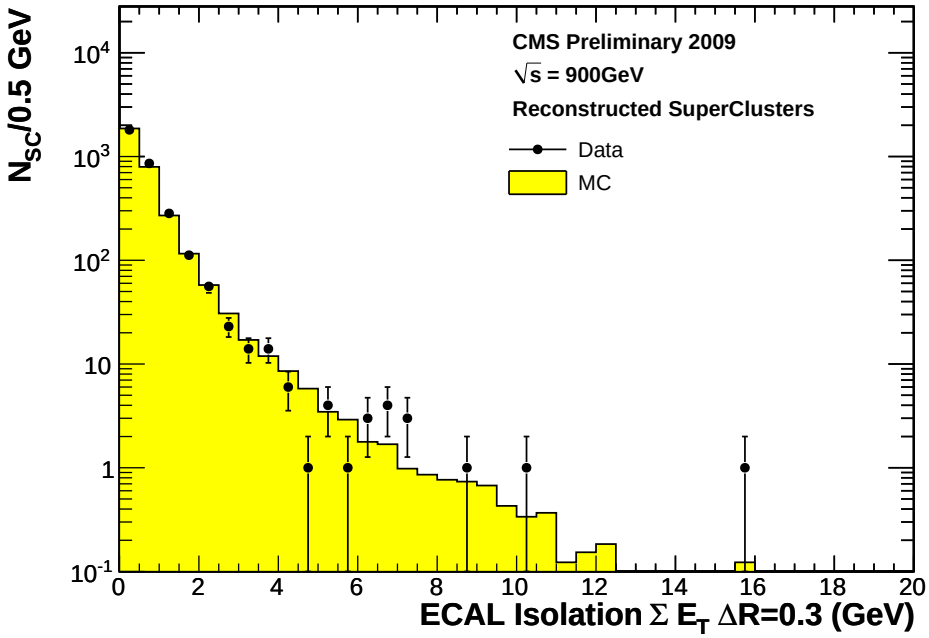

Figure 21: ECAL isolation distribution for superclusters. The black points correspond to data and the histogram to simulated minimum bias events.

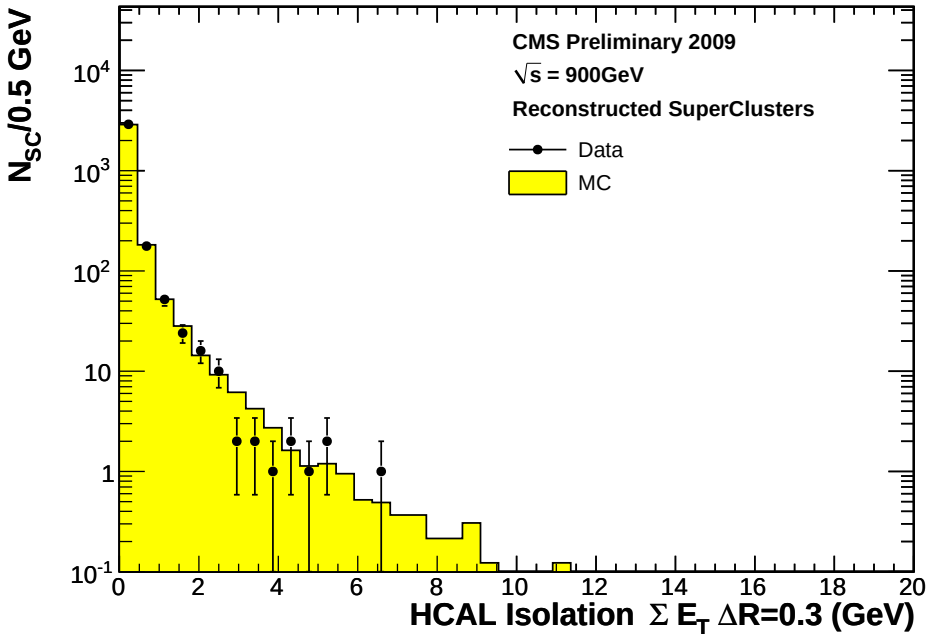

Figure 22: HCAL isolation distribution for superclusters. The black points correspond to data and the histogram to simulated minimum bias events.

used.

For this study electron candidates are required to lie within the pseudorapidity range $|\eta| < 1.4442$ or $1.566 < |\eta| < 2.5$ to avoid the barrel endcap transition region.

Fig. 23 shows the distribution of track isolation, Fig. 24 shows the distribution of ECAL isolation and Fig. 25 shows the distribution of HCAL isolation.

A good agreement is found between data and Monte Carlo.

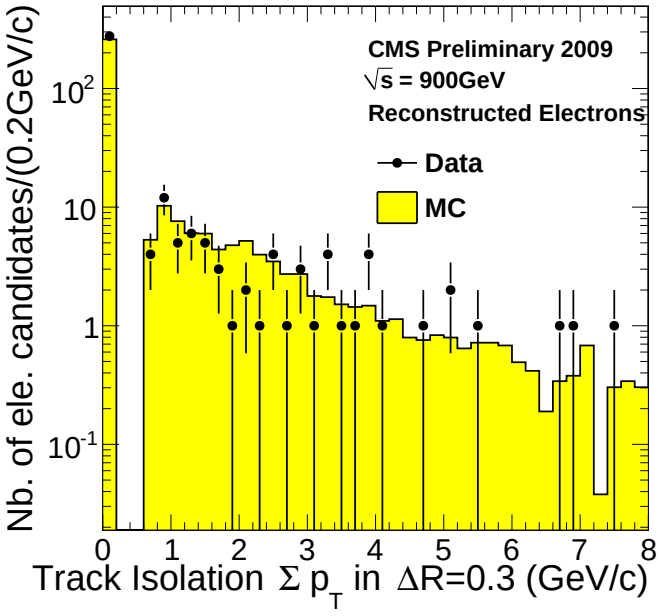

Figure 23: Track isolation distribution for electron candidates in both EB and EE. The black points correspond to data and the histogram to simulated minimum bias events.

7 Summary

Using the first proton-proton collision data collected with the CMS detector in 2009 at a center of mass energy of 900 GeV comparisons between data and simulation were carried out for ECAL clusters, reconstructed GSF tracks, reconstructed electron candidates and tracker, ECAL and HCAL isolation variables for electromagnetic candidates. Due to the limited statistics of the available sample, comparison has been carried out for objects in absence of identification requirements, so the sample is dominated by background (i.e. fakes).

All kinematic and identification variables which have been considered show a good agreement between data and Monte Carlo, leading to the conclusion that the response of the subdetectors is well modeled in the simulation and that the algorithms designed and optimized in the simulation show a behavior consistent with what is expected.

The commissioning of the electromagnetic physics objects will continue with the upcoming LHC data at higher center of mass energies, with the advent of a large statistics of W and Z bosons decaying into energetic and isolated electrons.

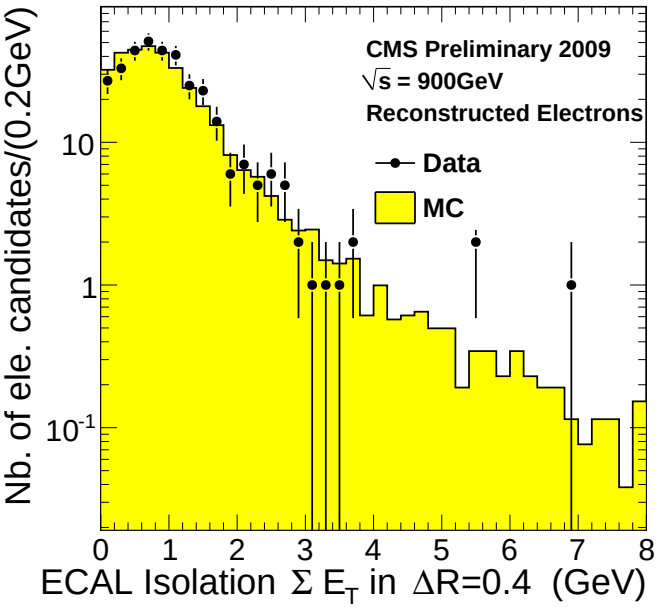

Figure 24: Ecal isolation distribution for all reconstructed electron candidates. The black points correspond to data and the histogram to simulated minimum bias events.

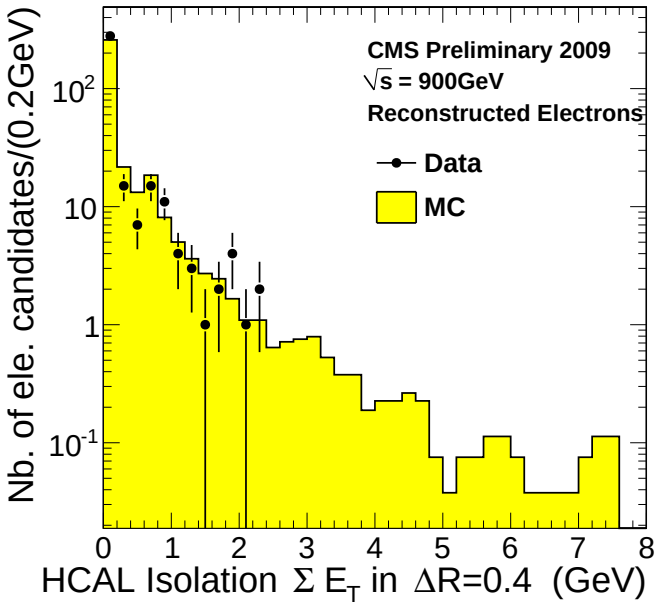

Figure 25: HCAL isolation distribution for all electron candidates. The black points correspond to data and the histogram to simulated minimum bias events.

References

[1] **CMS** Collaboration, "The CMS experiment at the CERN LHC", *JINST* **3** (2008) S08004. doi:10.1088/1748-0221/3/08/S08004.

[2] **CMS** Collaboration, "Tracking and Vertexing Results from First Collisions", *CMS PAS* **TRK-2010/001** (2010).

[3] S. Agostinelli, J. Allison, K. Amako et al., "G4–a simulation toolkit", *Nuclear Instruments and Methods in Physics Research Section A: Accelerators, Spectrometers, Detectors and Associated Equipment* **506** (2003), no. 3, 250 – 303. doi:10.1016/S0168-9002(03)01368-8.

[4] T. Sjostrand, P. Eden, C. Friberg et al., "High-Energy-Physics Event Generation with PYTHIA 6.1", *Comput. Phys. Commun.* **135** (2001) 238.

[5] **CMS** Collaboration, "CMS physics : Technical Design Report", *CERN/LHCC* **CERN-LHCC-2006-001** (2006).

[6] W. Adam, R. Fruhwirth, A. Strandlie, T. Todorov, "Reconstructions of Electrons with the Gaussian-Sum Filter in the CMS Tracker at the LHC", *J. Phys. G: Nucl. Part. Phys.* **31** (2005) N9–N20.

[7] S. Baffioni et al., "Electron reconstruction in CMS", *Eur. Phys. J. C* **49** (2007), no. 3, 1099.

[8] **CMS** Collaboration, "Commissioning of the Particle-flow Event Reconstruction with the first LHC collisions recorded in the CMS detector", *CMS PAS* **PFT-2010/001** (2010).

[9] N. Marinelli, "Track finding and identification of converted photons", *CMS NOTE* **2006/005** (2006).

A Event display of a candidate conversion

Figure 26 shows the R$-\phi$ view of a fully reconstructed conversion candidate. The converted γ is well isolated and well balanced in ϕ by the hadronic activity. The main characteristics of the electrons of the converted γ are summarized in Table 2. The measured energies of the ECAL superclusters may not be very accurate because both electrons are in the barrel-endcap transition region while the GSF tracks are expected to give a better estimate of the electron momenta.

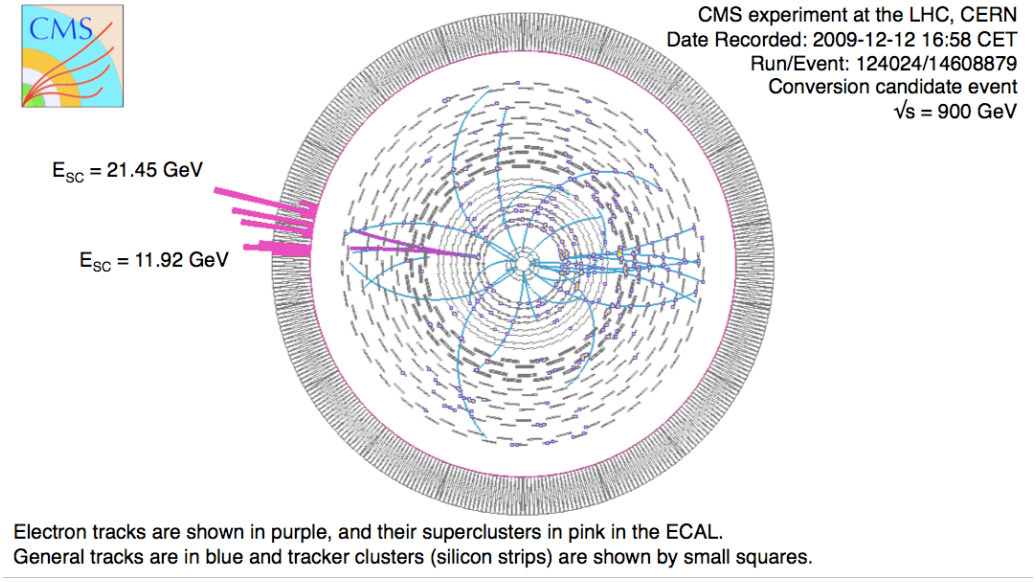

Figure 26: R$-\phi$ view of a conversion candidate. Reconstructed electron tracks (purple), general tracks (blue) and energy deposits in the ECAL (pink) are shown.

	q	1^{st} hit position x,y,z (cm)	p_{in} (GeV/c)	E_{SC} (GeV)	η_{SC}	ϕ_{SC}	E/p	E_{seed}/p_{out}	f_{brem}	mva
e_1	+1	-26.9859,4.17588,-62.7382	14.92	21.45	-1.567	2.941	1.438	0.995	0.351	0.743
e_2	-1	-26.9857,4.17458,-62.7987	55.53	11.92	-1.563	3.080	0.215	0.915	0.765	0.621

Table 2: Characteristics of the two electron candidates of the fully reconstructed conversion. The last column shows the multivariate analysis variable (mva) which is computed for all electron candidates and is used for the preselection of track driven electrons.

B Observation of the $\pi^0 \longrightarrow \gamma\gamma$ signal with one leg reconstructed from conversion candidates in 900 GeV data

Using the first CMS collision data collected at 900 GeV center of mass energy we also looked for the signal due to π^0s decaying into 2 photons, where one of the two legs is reconstructed as a conversion. Only tracker driven conversion reconstruction [2] was used since only low p_T photons (< 3 GeV/c) were involved and most of the conversion tracks do not reach the electromagnetic calorimeter. At such low transverse momenta ECAL seeded conversion reconstruction [9] has a very low efficiency, being optimized for conversions of p_T greater than 10 GeV/c.

The event selection is the same described in section 2.

The π^0 candidate selection starts by applying the following requirements to identify a conversion candidate:

- a reconstructed tracker conversion candidate [2] should be present;
- the absolute value of the distance of minimum approach between the two tracks is required to be less than 0.04 cm;
- the value of $|\Delta cot\theta|$ between the two tracks at the innermost state is required to be less than 0.05.

We then require the presence of a cluster, as reconstructed by the island algorithm [5], with $p_T > 0.3$ GeV/c in the ECAL barrel; we finally require that the total transverse momentum of the π^0 candidate should be greater than 0.85 GeV/c. The ECAL cluster energy is given by the sum of the reconstructed energies in the individual ECAL crystals without applying a correction for possible incomplete containment.

Figure 27 shows the invariant mass distribution of the π^0 candidates for the data and the minimum bias simulation. The simulation is normalized to the same number of selected conversion candidates in the data. A fit to the data points, obtained with a Gaussian distribution summed with a second order polynomial to describe the combinatorial background component, is also shown.

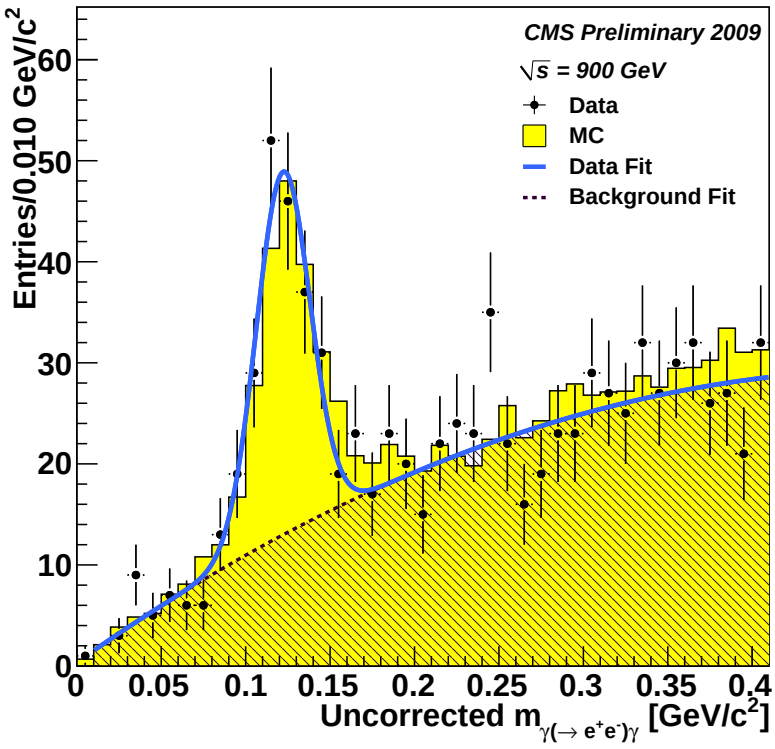

Figure 27: Invariant mass of π^0 candidates selected as discussed in the text: data (black points) are superimposed on the MC expectation (filled yellow histogram). Monte Carlo is normalized to the same number of selected conversion candidates. A fit to the data points, obtained with a Gaussian distribution summed with a second order polynomial to describe the combinatorial background component, is also shown.

The signal yield and the signal-to-background ratio are well reproduced by the simulation. The shift in the mass is well reproduced in the MC and is consistent with what is observed in the non-converted two-photon decays.